

Metallic and Deconfined Quantum Criticality in Dirac Systems

Zi Hong Liu,¹ Matthias Vojta,² Fakher F. Assaad,¹ and Lukas Janssen²

¹*Institut für Theoretische Physik und Astrophysik and Würzburg-Dresden Cluster of Excellence ct.qmat, Universität Würzburg, 97074 Würzburg, Germany*

²*Institut für Theoretische Physik and Würzburg-Dresden Cluster of Excellence ct.qmat, Technische Universität Dresden, 01062 Dresden, Germany*

Motivated by the physics of spin-orbital liquids, we study a model of interacting Dirac fermions on a bilayer honeycomb lattice at half filling, featuring an explicit global $\text{SO}(3) \times \text{U}(1)$ symmetry. Using large-scale auxiliary-field quantum Monte Carlo (QMC) simulations, we locate two zero-temperature phase transitions as function of increasing interaction strength. First, we observe a continuous transition from the weakly-interacting semimetal to a different semimetallic phase in which the $\text{SO}(3)$ symmetry is spontaneously broken and where two out of three Dirac cones acquire a mass gap. The associated quantum critical point can be understood in terms of a Gross-Neveu- $\text{SO}(3)$ theory. Second, we subsequently observe a transition towards an insulating phase in which the $\text{SO}(3)$ symmetry is restored and the $\text{U}(1)$ symmetry is spontaneously broken. While strongly first order at the mean-field level, the QMC data is consistent with a direct and continuous transition. It is thus a candidate for a new type of deconfined quantum critical point that features gapless fermionic degrees of freedom.

Metallic quantum criticality corresponds to the spontaneous breaking of a symmetry in a metallic environment triggered by varying a non-thermal control parameter such as doping, magnetic field, or pressure [1–3]. Order-parameter fluctuations often induce non-Fermi-liquid behavior in a temperature-versus-control-parameter window of the phase diagram [4–6]. Metallic quantum criticality is pivotal in understanding anomalous transport and strange-metal behavior in strongly correlated materials, such as heavy-fermion compounds [7] and Cu- and Fe-based high-temperature superconductors [8, 9]. In spite of extensive efforts [1–3, 10–17], a controlled analytical treatment of this problem in the presence of a Fermi surface remains a major challenge. The main difficulty is to tame the strong quantum fluctuations that arise from the abundance of gapless particle-hole modes near the Fermi surface. From the numerical point of view [18], the fact that these transitions are characterized by dynamical critical exponents $z > 1$ impedes the ability to reach sufficiently low temperatures on large lattices [19].

Dirac systems, in contrast, have emergent Lorentz symmetry: Space and time are interchangeable and $z = 1$. Furthermore, instead of an extended Fermi surface, they feature isolated Fermi points. In the past years, there has been a considerable amount of work investigating dynamical mass generation in these systems. The understanding of such transitions relies on the Gross-Neveu-Yukawa theory, in which an order-parameter field of given symmetry is coupled to a fermion-mass term in the same symmetry sector [20]. Various instances of these transitions have been studied from the perspective of high-energy [21–25] and solid-state [26–36] physics. In all of the above examples, the quantum critical points separate Dirac semimetallic states from insulating states with a full gap in the fermionic spectrum. Dirac systems can, however, in principle also support relativistic quantum critical points between two distinct semimetallic phases. This possibility was recently scrutinized in the context of a frustrated spin-orbital model, in which case the fermion degrees of freedom arise from a spin fractionalization mechanism [37]. If such a transition is real-

izable, it would represent a Dirac *avatar* of metallic quantum criticality that may be more easily accessible to both numerical and field-theoretical analyses.

In this Letter, we investigate a two-dimensional lattice model of interacting fermions designed to feature such a semimetal-to-semimetal quantum critical point. Inspired by Ref. 37, we study the Hamiltonian

$$H = -t \sum_{\langle i,j \rangle} c_{i\sigma\lambda}^\dagger c_{j\sigma\lambda} - J \sum_{i\alpha} \left(c_{i\sigma\lambda}^\dagger K_{\sigma\sigma'}^\alpha \tau_{\lambda\lambda'}^z c_{i\sigma'\lambda} \right)^2, \quad (1)$$

where $\langle i, j \rangle$ denote pairs of nearest-neighbor sites of a honeycomb lattice, $\lambda = 1, 2$ is an additional layer index, and summation over repeated indices is implied. Further, $\sigma = 1, 2, 3$ is an $\text{SO}(3)$ flavor index, $(K^\alpha)_{\sigma\sigma'} = -i\epsilon_{\alpha\sigma\sigma'}$ are the generators of $\text{SO}(3)$, and $\tau^{x,y,z}$ are Pauli matrices. The model is particle-hole symmetric such that zero chemical potential corresponds to half filling.

The interaction term in Eq. (1) is chosen such that the $\text{SO}(3)$ symmetry may be spontaneously broken, resulting in a three-component order parameter $\mathbf{m} = (m_1, m_2, m_3)^\top$. For a single layer, this leads to the low-energy effective Hamiltonian

$$\mathcal{H} = \Psi_\sigma^\dagger [i\gamma_0 \gamma_j p_j \delta_{\sigma\sigma'} + m_\alpha (K^\alpha)_{\sigma\sigma'} \gamma_0] \Psi_{\sigma'}, \quad (2)$$

where $i\gamma_0 \gamma_j p_j$ is the usual Dirac Hamiltonian in two spatial dimensions, $j = 1, 2$. The operator $\mathbf{K}_{\sigma\sigma'} \gamma_0$ anticommutes with the Dirac Hamiltonian, and as such may be thought of as a mass term, but since $(\mathbf{m} \cdot \mathbf{K})\mathbf{v} = i\mathbf{m} \times \mathbf{v}$ for an arbitrary three-component vector \mathbf{v} , only two out of three Dirac cones will acquire a gap. In particular, the wavefunction $\Psi_\sigma(\tau, \mathbf{x}) \equiv m_\sigma \psi(\tau, \mathbf{x})$ will correspond to the massless Dirac fermions. The dynamical generation of such term hence corresponds to metallic quantum criticality in a Dirac system, in contrast to the situation in related models that feature metal-insulator transitions [33, 38]. Equation (2) encodes a new class of Gross-Neveu (GN) transitions dubbed GN- $\text{SO}(3)$ that have recently been studied using approximate analytical techniques [39].

The microscopic model (1) is amenable to large-scale negative-sign-free auxiliary-field quantum Monte Carlo

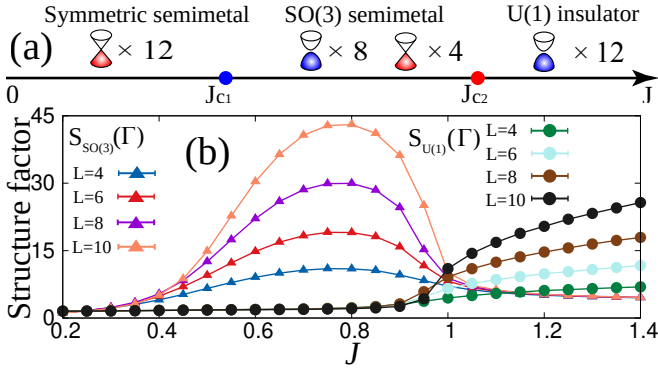


FIG. 1. (a) Ground-state phase diagram of the model (1) as function of interaction strength J , obtained from AFQMC simulations. The semimetal-to-semimetal transition at J_{c1} is continuous and can be understood in terms of a GN-SO(3) field theory. The semimetal-to-insulator transition at J_{c2} , while strongly first order at the mean-field level, appears continuous. (b) Variation of SO(3) and U(1) structure factors $S_{SO(3)}(k = \Gamma)$ and $S_{U(1)}(k = \Gamma)$ as function of J for different lattice sizes. Extensive structure factors reflect spontaneous symmetry breaking.

(AFQMC) simulations [40–42], and Fig. 1 summarizes our key results at zero temperature and half band filling. In the weakly-interacting limit, the model features a stable semimetallic phase, characterized by $N = 12$ irreducible Dirac cones located at the corners K and K' of the first Brillouin zone. At intermediate couplings, a semimetallic SO(3)-symmetry-broken phase with flavor order indeed emerges, in which two thirds of the Dirac cones are gapped out, while one third remains gapless. Remarkably, upon further increasing the interaction strength, we encounter another phase, which now is insulating and displays spontaneously broken U(1) symmetry, corresponding to emergent interlayer coherence. The first transition is continuous at the mean-field level, and the effects of quantum fluctuations can be understood in terms of the GN-SO(3) field theory studied in [39]. The second transition is strongly first order at the mean-field level, as is usual for direct transitions between states that break different symmetries. Our numerical results, however, indicate that quantum fluctuations render this order-to-order transition continuous (but we cannot exclude it to be weakly first order). It hence likely represents an example of a new type of deconfined quantum critical point [43] featuring gapless fermionic degrees of freedom [44].

Mean-field analysis. Our mean-field approximation relies on the identity

$$-J \sum_{i\alpha} \left(c_i^\dagger K^\alpha \tau^z c_i \right)^2 = -J \sum_{i\alpha\lambda} \left(c_{i\lambda}^\dagger K^\alpha c_{i\lambda} \right)^2 + 2J \sum_{i\alpha\sigma\sigma'} |\epsilon_{\alpha\sigma\sigma'}| \left(\Delta_{i\sigma}^\dagger \Delta_{i\sigma'} + n_{i\sigma}^\dagger n_{i\sigma'} \right) \quad (3)$$

with $\Delta_{i\sigma}^\dagger = c_{i\sigma 1}^\dagger c_{i\sigma 2}^\dagger$ and $n_{i\sigma}^\dagger = c_{i\sigma 1}^\dagger c_{i\sigma 2}$. The above allows us to define an SO(3) order parameter for staggered flavor order, $m_\alpha/2 = (-1)^i \langle c_{i\lambda}^\dagger K^\alpha c_{i\lambda} \rangle$, and a U(1) order parameter for interlayer coherence, $V/2 = (-1)^i \langle n_{i\sigma}^\dagger \rangle$. In the spirit

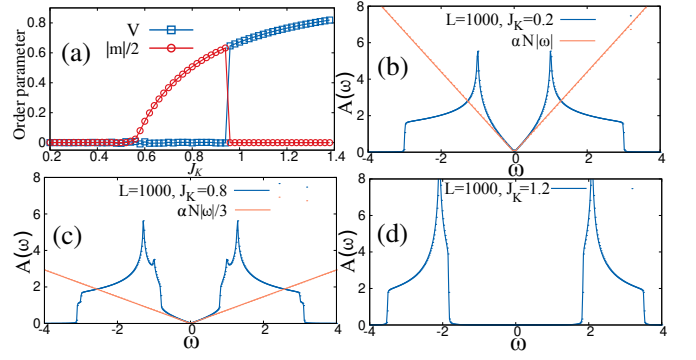


FIG. 2. Mean-field results for the model (1), obtained on an $L = 60$ lattice. (a) SO(3) and U(1) order parameters m_α and V as function of J . (b,c,d) Single-particle density of states for representative fixed values of J in the three phases.

of the continuum limit of Eq. (2), the order parameters map onto $\Psi_{\sigma\lambda}^\dagger \gamma_0 K_{\sigma\sigma'}^\alpha \Psi_{\sigma'\lambda}$ and $\Psi_{\sigma\lambda}^\dagger \gamma_0 \tau_{\lambda\lambda'}^x \Psi_{\sigma\lambda'}$, respectively, and open partial and full gaps in the fermion spectrum. Since in the QMC calculations we have not observed superconductivity, we omit the corresponding term in the mean-field approximation. For details of the calculations, see [45].

Figure 2(a) shows the mean-field order parameters as function of J/t . The symmetric Dirac phase has a low-energy density of states $N(\omega) = \alpha N |\omega|$ that changes to $N(\omega) = \alpha \frac{N}{3} |\omega|$ in the SO(3)-broken phase, consistent with two out of three Dirac cones acquiring a mass gap, Figs. 2(b,c). At larger values of J/t , we observe a strong first-order transition to a U(1)-broken state whose fermion spectrum is gapped, Fig. 2(d).

QMC simulations. We have used the ALF [46] implementation of AFQMC, and employed the finite-temperature grand canonical and projective approaches. We used a symmetric Suzuki-Trotter decomposition to control the systematic error in observables [47, 48] and adopted an imaginary time step $\Delta\tau t = 0.05$ for the finite-temperature algorithm and $\Delta\tau t = 0.1$ for the projective formulation.

The absence of a negative-sign problem for positive values of J stems from a particular time-reversal symmetry that relies on the bilayer structure of the model. After a Hubbard-Stratonovich (HS) decomposition of the perfect-square interaction term, the resulting one-body Hamiltonian, for a given space-time configuration of HS fields, has a time-reversal symmetry, defined as $T^{-1} z c_{i\sigma\lambda}^\dagger T = \bar{z} i \tau_{\lambda\lambda'}^y c_{i\sigma\lambda'}^\dagger$. This stems from the fact that the SO(3) generators are purely imaginary. Hence, the eigenvalues of the fermion matrix occur in complex conjugate pairs such that positivity of the determinant follows [49]. To minimize size effects we follow Ref. [50] and thread the lattice with a magnetic flux quantum of opposite sign in the two layers [45]. It is interesting to note that introducing a chemical potential will not break this time-reversal symmetry, and simulations at finite doping are amenable to negative-sign-free QMC.

QMC results. We carry out QMC simulations of the model (1) on $L = 6, 9, 12, 15, 18$ lattices with $6L^2$ orbitals

per honeycomb layer, set $t = 1$, and scan as function of J . Our results are summarized schematically in Fig. 1(a). Each phase is characterized by spontaneous symmetry breaking and diverging structure factor at $\mathbf{Q} = \Gamma$, Fig. 1(b). To detect SO(3) symmetry breaking we consider $S_{\text{SO}(3)}(\mathbf{k}, \tau) = \sum_{r_{ij,\lambda}} e^{-i\mathbf{k}\cdot\mathbf{r}_{ij}} \langle c_{i,\lambda}^\dagger(\tau) \mathbf{K} c_{i,\lambda}(\tau) \cdot c_{j,\lambda}^\dagger(0) \mathbf{K} c_{j,\lambda}(0) \rangle$ and for the U(1) phase, $S_{\text{U}(1)}(\mathbf{k}, \tau) = \frac{1}{2} \sum_{r_{ij,\sigma}} e^{-i\mathbf{k}\cdot\mathbf{r}_{ij}} \langle n_{i,\sigma}^\dagger(\tau) n_{j,\sigma} + n_{j,\sigma}(\tau) n_{i,\sigma}^\dagger \rangle$. Here, \mathbf{r}_{ij} corresponds to the distance between the unit cells of i and j .

Each phase has a distinct signature in the single-particle spectral function $A(\mathbf{k}, \omega)$. We extract this quantity from the ground-state imaginary-time-displaced fermion Green's functions $G(\mathbf{k}, \tau) = \frac{1}{\pi} \int d\omega e^{-\tau\omega} A(\mathbf{k}, \omega)$ by using the ALF [46] implementation of the stochastic analytic continuation method [51]. In Fig. 3(b), in the symmetric phase, the fermion spectrum reveals semimetallic behavior. In Fig. 3(c), in the SO(3)-broken phase, part of low-energy spectral weight is removed, but a finite weight at the Dirac point is still apparent. To demonstrate this explicitly, we make use of the fact that for a gapless mode, the quasiparticle residue reads $Z(\mathbf{k}) = 2 \text{Tr} G(\mathbf{k}, \beta/2)$ [52]. We use a $\beta = L$ scaling and extrapolate Z to the thermodynamic limit, see Fig. 3(a). In the semimetallic phase, the quasiparticle residue extrapolates to the free Dirac-metal value $Z(k = K) = 6$. In the SO(3)-symmetry-breaking phase, using a polynomial fit, we obtain the estimated quasiparticle residue $Z(k = K) = 1.9(1)$. The ratio of the quasiparticle weights is close to three, as expected from the gapping out of 2/3 of the Dirac cones. Finally in the U(1)-broken phase, the spectrum shows a full gap, Fig. 3(d).

The two phase transition points are located by monitoring the renormalization-group (RG) invariant correlation ratio [53] $R_c = 1 - \frac{S(\mathbf{k}=\mathbf{Q}+d\mathbf{k}, \tau=0)}{S(\mathbf{k}=\mathbf{Q}, \tau=0)}$, where $S(\mathbf{k}, \tau=0)$ is the structure factor of either the SO(3) or the U(1) order, \mathbf{Q} is the ordering wavevector and $d\mathbf{k}$ the smallest momentum on the considered lattice.

To investigate the first phase transition, we will assume $z = 1$ and adopt a $\beta = L$ scaling within the finite-temperature AFQMC algorithm. As apparent in Fig. 4(a), this phase transition involves only SO(3) symmetry breaking since a clear crossing is observed in $R_c^{\text{SO}(3)}$. On the other hand, $R_c^{\text{U}(1)}$ vanishes for increasing system size, thus excluding long-range U(1) order in the considered parameter range. In the quantum critical region, we expect the correlation ratio $R_c^{\text{SO}(3)}$ to obey the finite-size scaling (FSS) ansatz [54] $R_c^{\text{SO}(3)}(J, L) = f_0^R(jL^{1/\nu}) + L^{-\omega} f_1^R(jL^{1/\nu})$, where $j = J - J_{c1}$. f_0^R and f_1^R are scaling functions and ω is the leading-correction-to-scaling exponent. To extract the values of the critical exponent ν and the critical point J_{c1} , we fit the scaling function $f_0^R(jL^{1/\nu})$ to a polynomial [45]. In our simulations, the crossing point in the $R_c^{\text{SO}(3)}$ data becomes size independent within our accuracy. Hence for $L \geq 12$, corrections to scaling can be omitted. Our results are consistent with $1/\nu = 0.906(35)$ and $J_{c1} = 0.461(1)$. The data collapse of $R_c^{\text{SO}(3)}(J, L)$ is depicted in Fig. 4(b). The bosonic, η_ϕ , and fermionic, η_ψ , anomalous dimensions are related to the

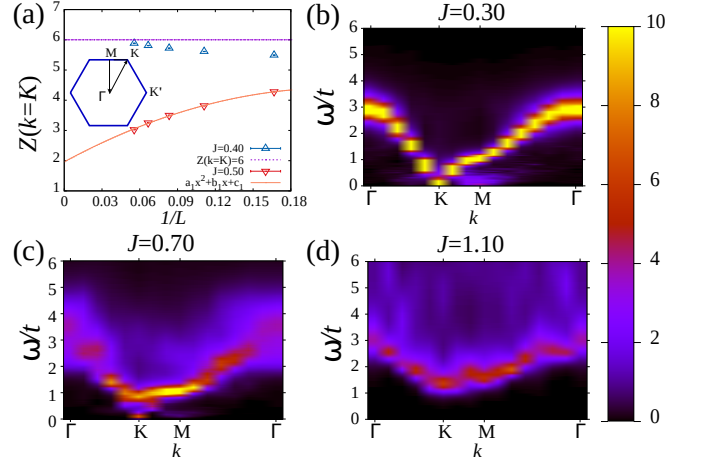


FIG. 3. (a) Quasiparticle weight $Z(k = K)$ as a function of inverse system size, $1/L$, in the symmetric ($J = 0.40$) and SO(3)-broken ($J = 0.50$) phases, respectively. The polynomial fitting of the second curve yields $Z = 1.9(1)$ for $L \rightarrow \infty$. (b-d) Fermion spectral function $A(\mathbf{k}, \omega)$ along the path in momentum space shown in the inset of (a), shown for (b) the symmetric phase at $J = 0.30$, (c) the SO(3)-broken phase at $J = 0.70$, and (d) the U(1)-broken phase at $J = 1.10$. Finite weight at the Dirac point is visible in (b) and (c), corresponding to semimetallic behavior, albeit with a reduced low-energy weight in the case of the SO(3)-broken semimetal (c). The low-energy weight at the M point especially visible in (b) is an artifact of the magnetic flux and does not survive the thermodynamic limit [45].

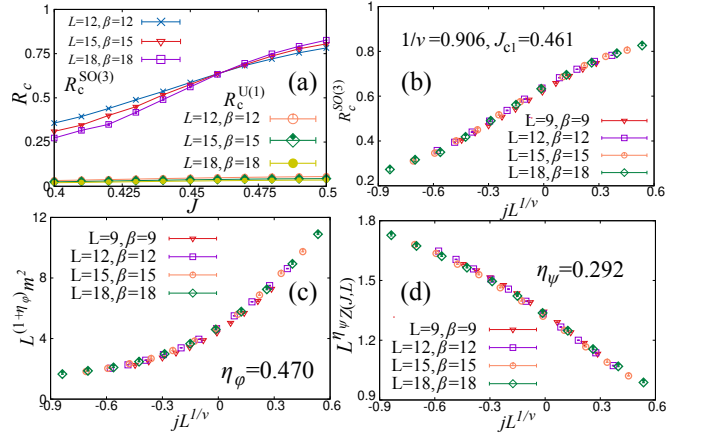


FIG. 4. QMC characterization of GN-SO(3) transition at J_{c1} . (a) Correlation ratios of the U(1) and SO(3) order parameters. (b-d): Scaling collapse near $J_{c1} = 0.461$ of (b) correlation ratio $R_c^{\text{SO}(3)}$, (c) order parameter m^2 and (d) fermion quasiparticle weight Z , as function of $jL^{1/\nu}$, with $j = J - J_{c1}$ and ν the correlation-length exponent.

FSS ansatz of the SO(3) order parameter $m^2 = S_{\text{SO}(3)}(\mathbf{Q}, \tau = 0)/L^2$ and $Z(J, L) = G(J, L)/G(0, L)$, where $G(J, L) = \frac{1}{6} \sum_{\sigma,\lambda} \langle c_{0\sigma\lambda}^\dagger(\beta/2) c_{0\sigma\lambda}(0) \rangle$ at interaction strength J . At the critical point, and neglecting corrections to scaling, these two quantities scale as $m_{\text{SO}(3)}^2(j, L) = L^{-(1+\eta_\phi)} f^m(jL^{1/\nu}) = L^{-(1+\eta_\phi)} \tilde{f}^m(R_c^{\text{SO}(3)}(J, L))$ and $Z(J, L) = L^{-\eta_\psi} f^z(jL^{1/\nu}) =$

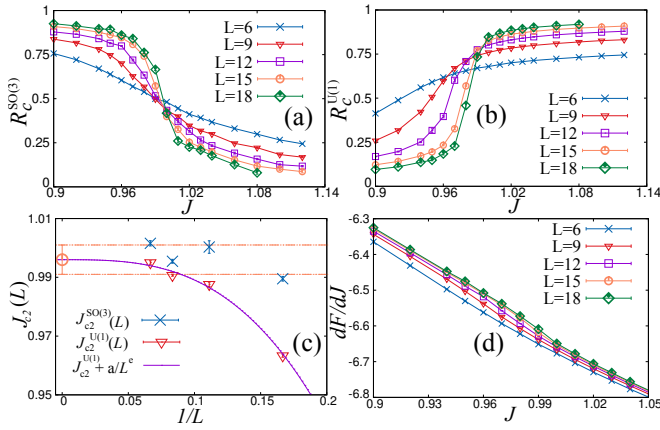


FIG. 5. QMC characterization of SO(3)-U(1) transition at J_{c2} . (a,b) Correlation ratios as function of J across transition. (c) Finite-size critical couplings $J_{c2}^{SO(3)/U(1)}(L)$ as function of $1/L$. While $J_{c2}^{U(1)}(L)$ increases with system size, $J_{c2}^{SO(3)}(L)$ stabilizes within our accuracy as $L \geq 9$. By extrapolating $J_{c2}^{U(1)}(L)$ using the power-law ansatz $J_{c2} + a/L^e$, we obtain the estimate $J_{c2} = 1.0013(18)$. (d) First derivative of free energy dF/dJ near J_{c2} , showing no discontinuity within our accuracy.

$L^{-\eta_\psi} \tilde{r}^z (R_c^{SO(3)}(J, L))$ [33]. Here we use the correlation ratio $R_c^{SO(3)}(J, L)$ as a dimensionless quantity to replace the variable $jL^{1/\nu}$ so as to reduce the number of fit variables. Following the regression result of the scaling function, we obtain the estimates $\eta_\phi = 0.470(13)$ and $\eta_\psi = 0.292(10)$. Figures 4(c,d) show the data collapse using the estimated exponents. Consistent results are obtained when collapsing the data with respect to $jL^{1/\nu}$ with ν [45].

At the mean-field level, the transition between the SO(3)-broken and U(1)-broken states is strongly first order. However, the QMC results for $R_c^{SO(3)}$ and $R_c^{U(1)}$ do not suggest a strong first-order transition, Figs. 5(a,b). To assess if there is a coexistence regime, we carry out a crossing-point analysis to determine the coupling at which the SO(3) [U(1)] order is suppressed (appears). We determine the finite-size critical couplings $J_{c2}^{SO(3)/U(1)}(L)$ by $R_c(J_{c2}(L), L) = R_c(J_{c2}(L), L+3)$. As the system size $L \rightarrow \infty$, the finite-size critical couplings $J_{c2}^{SO(3)/U(1)}(L)$ scale as $J_{c2}^{SO(3)/U(1)} + aL^{-e}$, where $e = 1/\nu + \omega$ and a is a nonuniversal constant. The results, plotted in Fig. 5(c), suggests that within our accuracy, $J_{c2}^{SO(3)} = J_{c2}^{U(1)}$. In Fig. 5(d), we plot the first derivative of the free energy with respect to J . Within our accuracy, we do not observe a discontinuity expected for a first-order transition. Consistent estimates of the correlation-length exponent from the U(1) and SO(3) structure factors are reported in [45].

Discussion and summary. We have introduced a model Hamiltonian, amenable to large-scale negative-sign-free QMC simulations, that supports metallic quantum criticality in Dirac systems. The SO(3) order generates mass in two out of three Dirac cones. Using a FSS analysis, we estimate the critical

exponents of the SO(3)-ordering transition

$$1/\nu = 0.906(35), \quad \eta_\phi = 0.470(13), \quad \eta_\psi = 0.292(10) \quad (4)$$

for the correlation-length exponent and the boson and fermion anomalous dimensions. We expect our model to fall into the GN-SO(3) universality class, with $N = 12$ two-component Dirac fermions. Calculations in [39], based on ϵ expansion, large- N , and functional renormalization-group approaches, yield exponents that differ from our estimates: $1/\nu = 0.93(4)$, $\eta_\phi = 0.83(4)$, $\eta_\psi = 0.041(12)$. While we cannot exclude that the discrepancy stems from finite-size effects in the QMC or convergence issues in the analytical approaches, they are large enough to speculate if topological defects in the field configurations—not included in [39]—play a role, see below. Note that within the QMC approach one can in principle systematically carry out calculations at $N = 12n$ and thereby test the validity of the large- N approach.

At larger couplings, the model shows an order-to-order transition between the SO(3) semimetal and a U(1) insulator. While at the mean-field level this transition is strongly first order, the QMC data on lattice sizes with up to 18×18 unit cells can be interpreted in terms of a continuous and direct transition, thereby providing an instance of a new type of deconfined quantum critical point [43] featuring gapless fermionic degrees of freedom [44]. Clearly, we cannot exclude the possibility of a weakly-first-order transition, in which, as suggested in the realm of deconfined criticality, the correlation length grows beyond the accessible system size due to the proximity of a critical fixed point in the complex-coupling plane [55–61].

The discrepancy between the QMC critical exponents and those of Ref. 39, as well as the seemingly-continuous transition between the SO(3)-broken semimetal and U(1)-broken insulator leads us to ask the question if the topology of the SO(3) order parameter can play a role. For a given SO(3) mass term, $[\mathbf{m}(\mathbf{x}) \cdot \mathbf{K}] \gamma_0$, the wavefunction of the gapless Dirac cone reads $\Psi_{\sigma\lambda}(\mathbf{x}) = m_\sigma(\mathbf{x}) \psi_\lambda(\mathbf{x})$. Consider an interface where on both sides the vectors \mathbf{m} are orthogonal to each other. Due to the orthogonality of the vectors \mathbf{m} , the wavefunction vanishes at the interface and a particle will not be able to cross it. The topological excitation of the SO(3) order parameter in two spatial dimensions is a skyrmion. In its core the SO(3) order parameter is given by \mathbf{m}_c and at infinity by $-\mathbf{m}_c$. The core is surrounded by a vortex in a plane perpendicular to \mathbf{m}_c that acts as an infinite potential barrier. As a consequence, we can foresee that a skyrmion of the SO(3) order parameter will trap charge in its core. Mean-calculations supporting this point of view are presented in [45]. Understanding if this *topological localization* is essential for the description of the observed phase transitions remains an open issue.

The phase diagram of our model contains two ordered phases with low-lying Goldstone modes. As mentioned above, it is possible to dope our system without encountering a negative-sign problem. Hence, numerical simulations aimed at understanding the nature of the doping-induced transitions to correlated metals (or superconductors [62]) should be feasible; these will be subject of future work.

The authors gratefully acknowledge the Gauss Centre for Supercomputing e.V. (www.gauss-centre.eu) for funding this project by providing computing time on the GCS Supercomputer SUPERMUC-NG at Leibniz Supercomputing Centre (www.lrz.de). This research has been supported by the Deutsche Forschungsgemeinschaft through the Würzburg-Dresden Cluster of Excellence on Complexity and Topology in Quantum Matter – *ct.qmat* (EXC 2147, Project No. 390858490), SFB 1170 on Topological and Correlated Electronics at Surfaces and Interfaces (Project No. 258499086), SFB 1143 on Correlated Magnetism (Project No. 247310070), and the Emmy Noether Program (JA2306/4-1, Project No. 411750675)

-
- [1] J. A. Hertz, *Phys. Rev. B* **14**, 1165 (1976).
 [2] A. J. Millis, *Phys. Rev. B* **48**, 7183 (1993).
 [3] T. Moriya, *Spin fluctuations in itinerant electron magnetism* (Springer, Berlin, 2012).
 [4] W. Metzner, D. Rohe, and S. Andergassen, *Phys. Rev. Lett.* **91**, 066402 (2003).
 [5] T. Senthil, *Phys. Rev. B* **78**, 035103 (2008).
 [6] H. v. Löhneysen, A. Rosch, M. Vojta, and P. Wölfle, *Rev. Mod. Phys.* **79**, 1015 (2007).
 [7] P. Gegenwart, Q. Si, and F. Steglich, *Nat. Phys.* **4**, 186 (2008).
 [8] B. Keimer, S. A. Kivelson, M. R. Norman, S. Uchida, and J. Zaanen, *Nature* **518**, 179 (2015).
 [9] T. Shibauchi, A. Carrington, and Y. Matsuda, *Annu. Rev. Condens. Matter Phys.* **5**, 113 (2014).
 [10] A. Abanov, A. V. Chubukov, and J. Schmalian, *Adv. Phys.* **52**, 119 (2003).
 [11] A. Abanov and A. Chubukov, *Phys. Rev. Lett.* **93**, 255702 (2004).
 [12] M. A. Metlitski and S. Sachdev, *Phys. Rev. B* **82**, 075127 (2010).
 [13] M. A. Metlitski and S. Sachdev, *Phys. Rev. B* **82**, 075128 (2010).
 [14] S. Sur and S.-S. Lee, *Phys. Rev. B* **94**, 195135 (2016).
 [15] A. Schliefl, P. Lunts, and S.-S. Lee, *Phys. Rev. X* **7**, 021010 (2017).
 [16] S.-S. Lee, *Annu. Rev. Condens. Matter Phys.* **9**, 227 (2018).
 [17] A. Schliefl, P. Lunts, and S.-S. Lee, *Phys. Rev. B* **98**, 075140 (2018).
 [18] A. Chubukov, Solving metallic quantum criticality in a casino, Journal Club for Condensed Matter Physics, November 2018, DOI:10.36471/JCCM_November_2018_02.
 [19] X. Y. Xu, A. Klein, K. Sun, A. V. Chubukov, and Z. Y. Meng, *npj Quantum Mater.* **5**, 1 (2020).
 [20] J. Zinn-Justin, *Nucl. Phys. B* **367**, 105 (1991).
 [21] F. Gehring, H. Gies, and L. Janssen, *Phys. Rev. D* **92**, 085046 (2015).
 [22] N. Zerf, L. N. Mihaila, P. Marquard, I. F. Herbut, and M. M. Scherer, *Phys. Rev. D* **96**, 096010 (2017).
 [23] J. A. Gracey, *Phys. Rev. D* **97**, 105009 (2018).
 [24] L. Iliesiu, F. Kos, D. Poland, S. S. Pufu, and D. Simmons-Duffin, *J. High Energy Phys.* **01** (2018) 36.
 [25] E. Huffman and S. Chandrasekharan, *Phys. Rev. D* **101**, 074501 (2020).
 [26] I. F. Herbut, *Phys. Rev. Lett.* **97**, 146401 (2006).
 [27] I. F. Herbut, V. Juričić, and O. Vafek, *Phys. Rev. B* **80**, 075432 (2009).
 [28] L. Janssen and I. F. Herbut, *Phys. Rev. B* **89**, 205403 (2014).
 [29] F. F. Assaad and I. F. Herbut, *Phys. Rev. X* **3**, 031010 (2013).
 [30] F. Parisen Toldin, M. Hohenadler, F. F. Assaad, and I. F. Herbut, *Phys. Rev. B* **91**, 165108 (2015).
 [31] Y. Otsuka, K. Seki, S. Sorella, and S. Yunoki, *Phys. Rev. B* **98**, 035126 (2018).
 [32] T. C. Lang and A. M. Läuchli, *Phys. Rev. Lett.* **123**, 137602 (2019).
 [33] Y. Liu, Z. Wang, T. Sato, M. Hohenadler, C. Wang, W. Guo, and F. F. Assaad, *Nat. Commun.* **10**, 1 (2019).
 [34] Y. Liu, W. Wang, K. Sun, and Z. Y. Meng, *Phys. Rev. B* **101**, 064308 (2020).
 [35] X. Y. Xu and T. Grover, *Phys. Rev. Lett.* **126**, 217002 (2021).
 [36] Y. Liu, Z. Wang, T. Sato, W. Guo, and F. F. Assaad, *Phys. Rev. B* **104**, 035107 (2021).
 [37] U. F. P. Seifert, X.-Y. Dong, S. Chulliparambil, M. Vojta, H.-H. Tu, and L. Janssen, *Phys. Rev. Lett.* **125**, 257202 (2020).
 [38] Z. Wang, Y. Liu, T. Sato, M. Hohenadler, C. Wang, W. Guo, and F. F. Assaad, *Phys. Rev. Lett.* **126**, 205701 (2021).
 [39] S. Ray, B. Ihrig, D. Kruti, J. A. Gracey, M. M. Scherer, and L. Janssen, *Phys. Rev. B* **103**, 155160 (2021).
 [40] R. Blankenbecler, D. J. Scalapino, and R. L. Sugar, *Phys. Rev. D* **24**, 2278 (1981).
 [41] J. E. Hirsch, *Phys. Rev. B* **31**, 4403 (1985).
 [42] S. R. White, D. J. Scalapino, R. L. Sugar, E. Y. Loh, J. E. Gubernatis, and R. T. Scalettar, *Phys. Rev. B* **40**, 506 (1989).
 [43] T. Senthil, L. Balents, S. Sachdev, A. Vishwanath, and M. P. A. Fisher, *Phys. Rev. B* **70**, 144407 (2004).
 [44] L. Zou and D. Chowdhury, *Phys. Rev. Research* **2**, 023344 (2020).
 [45] See Supplemental Material, which includes Ref. [63], for technical details of the mean-field calculation, the effects of magnetic flux on the spectral function, finite-size scaling analyses, as well as a discussion of electron localization effects of topological defects of the SO(3) order parameter.
 [46] ALF Collaboration, F. F. Assaad, M. Bercx, F. Goth, A. Götz, J. S. Hofmann, E. Huffman, Z. Liu, F. Parisen Toldin, J. S. E. Portela, and J. Schwab, [arXiv:2012.11914](https://arxiv.org/abs/2012.11914).
 [47] M. Suzuki, *Commun. Math. Phys.* **51**, 183 (1976).
 [48] H. F. Trotter, *Proc. Am. Math. Soc.* **10**, 545 (1959).
 [49] C. Wu and S.-C. Zhang, *Phys. Rev. B* **71**, 155115 (2005).
 [50] F. F. Assaad, *Phys. Rev. B* **65**, 115104 (2002).
 [51] K. Beach, [arXiv:cond-mat/0403055](https://arxiv.org/abs/cond-mat/0403055).
 [52] M. Brunner, F. F. Assaad, and A. Muramatsu, *Phys. Rev. B* **62**, 15480 (2000).
 [53] R. K. Kaul, *Phys. Rev. Lett.* **115**, 157202 (2015).
 [54] M. Campostrini, A. Pelissetto, and E. Vicari, *Phys. Rev. B* **89**, 094516 (2014).
 [55] A. Nahum, J. T. Chalker, P. Serna, M. Ortuño, and A. M. Somoza, *Phys. Rev. X* **5**, 041048 (2015).
 [56] C. Wang, A. Nahum, M. A. Metlitski, C. Xu, and T. Senthil, *Phys. Rev. X* **7**, 031051 (2017).
 [57] P. Serna and A. Nahum, *Phys. Rev. B* **99**, 195110 (2019).
 [58] A. Nahum, *Phys. Rev. B* **102**, 201116 (2020).
 [59] R. Ma and C. Wang, *Phys. Rev. B* **102**, 020407 (2020).
 [60] V. Gorbenco, S. Rychkov, and B. Zan, *J. High Energy Phys.* **10** (2018) 108.
 [61] V. Gorbenco, S. Rychkov, and B. Zan, *SciPost Phys.* **5**, 50 (2018).
 [62] V. Kozii, Z. Bi, and J. Ruhman, *Phys. Rev. X* **9**, 031046 (2019).
 [63] H. Shao, W. Guo, and A. W. Sandvik, *Science* **352**, 213 (2016).

Supplemental Material for “Exotic quantum criticality in Dirac systems: Metallic and deconfined”

Zi Hong Liu,¹ Matthias Vojta,² Fakher F. Assaad,¹ and Lukas Janssen²

¹*Institut für Theoretische Physik und Astrophysik and Würzburg-Dresden Cluster of Excellence ct.qmat, Universität Würzburg, 97074 Würzburg, Germany*

²*Institut für Theoretische Physik and Würzburg-Dresden Cluster of Excellence ct.qmat, Technische Universität Dresden, 01062 Dresden, Germany*

(Dated: February 25, 2022)

MEAN-FIELD CALCULATION

In this section, we discuss the mean-field calculation of the lattice model (1). In the main text, we have introduced two mean-field order parameters for the SO(3), $m_\alpha/2 = (-1)^i \langle c_{i\lambda}^\dagger K^\alpha c_{i\lambda} \rangle$, and the U(1), $V/2 = (-1)^i \langle n_{i\sigma}^\dagger \rangle$, orders. On a bipartite lattice, $(-1)^i$ takes the value +1 (-1) on sublattice A (B). Starting from Eq. (3) of the main text, our mean-field approximation reads:

$$\begin{aligned} -J \sum_{i\alpha} \left(c_{i\alpha}^\dagger K^\alpha \tau_z c_i \right)^2 &\approx -J \sum_{i\alpha\lambda} m_\alpha c_{i,\lambda}^\dagger K^\alpha c_{i,\lambda} \\ &- JV \sum_{i\alpha\sigma\sigma'} |\epsilon_{\alpha\sigma\sigma'}| \left(n_{i\sigma'} + n_{i\sigma}^\dagger \right) \\ &+ J \sum_{i\alpha} \left(V^2 + \frac{\tilde{m}^2}{2} \right). \end{aligned} \quad (S1)$$

The mean-field Hamiltonian consists of the terms on the right-hand-side of the above equation, supplemented by the fermion hopping term. To proceed, let us define by $a_{\mathbf{R},\sigma,\lambda}^\dagger$ and $b_{\mathbf{R},\sigma,\lambda}^\dagger$ the electron creation operators on sublattices A and B, respectively, in the unit cell \mathbf{R} . After Fourier transformation to momentum space, we obtain:

$$\begin{aligned} H_{\text{MF}} &= -t \sum_{\mathbf{k}\sigma\lambda} \left(f(\mathbf{k}) a_{\mathbf{k}\sigma\lambda}^\dagger b_{\mathbf{k}\sigma\lambda} + \text{h.c.} \right) + 2J \sum_{\mathbf{k}\alpha} \left(V^2 + \frac{m^2}{2} \right) \\ &- J \sum_{\mathbf{k}\alpha\lambda} m_\alpha \left(a_{\mathbf{k}\lambda}^\dagger K^\alpha a_{\mathbf{k}\lambda} - b_{\mathbf{k}\lambda}^\dagger K^\alpha b_{\mathbf{k}\lambda} \right) \\ &- JV \sum_{\mathbf{k}\alpha\sigma\sigma'} |\epsilon_{\alpha\sigma\sigma'}| \left[\left(n_{\mathbf{k}\sigma}^{a\dagger} - n_{\mathbf{k}\sigma}^{b\dagger} \right) + \left(n_{\mathbf{k}\sigma}^a - n_{\mathbf{k}\sigma}^b \right) \right] \\ &= \sum_{\mathbf{k}} \hat{\psi}_{\mathbf{k}}^\dagger M_{\mathbf{k}} \hat{\psi}_{\mathbf{k}} + 2J \sum_{\mathbf{k}\alpha} \left(V^2 + \frac{\tilde{m}^2}{2} \right), \end{aligned} \quad (S2)$$

where we have introduced the 12-component spinor $\hat{\psi}_{\mathbf{k}}^\dagger = \left(\{a_{\mathbf{k},\sigma,\lambda}^\dagger\}, \{b_{\mathbf{k},\sigma,\lambda}^\dagger\} \right)$ and

$$M_{\mathbf{k}} = \begin{bmatrix} M_{\mathbf{k}}^{aa} & -t f(\mathbf{k}) \hat{I} \\ -t f^*(\mathbf{k}) \hat{I} & M_{\mathbf{k}}^{bb} \end{bmatrix} \quad (S3)$$

with $f(\mathbf{k}) = e^{-ik_x a} + e^{i(k_x/2)a + i(\sqrt{3}k_y/2)a} + e^{i(k_x/2)a - i(\sqrt{3}k_y/2)a}$ and

$$M_{\mathbf{k}}^{aa} = \begin{bmatrix} & iJm_3 & -iJm_2 & -2JV & & \\ -iJm_3 & & iJm_1 & & -2JV & \\ iJm_2 & -iJm_1 & & & & -2JV \\ -2JV & & & & iJm_3 & -iJm_2 \\ & -2JV & & -iJm_3 & & iJm_1 \\ & & -2JV & iJm_2 & -iJm_1 & \end{bmatrix}. \quad (S4)$$

Finally, $M_{\mathbf{k}}^{bb} = -M_{\mathbf{k}}^{aa}$.

The values of the mean-field order parameters are determined by self-consistent conditions, $\langle \partial H_{\text{MF}} / \partial V \rangle = \langle \partial H_{\text{MF}} / \partial m \rangle = 0$, that translate to:

$$m_\alpha = \frac{1}{2} \sum_{\lambda} \left(\langle a_{\mathbf{k},\lambda}^\dagger K^\alpha a_{\mathbf{k},\lambda} \rangle - \langle b_{\mathbf{k},\lambda}^\dagger K^\alpha b_{\mathbf{k},\lambda} \rangle \right), \quad (S5)$$

$$V = \frac{1}{4} \sum_{\mathbf{k}\alpha\sigma\sigma'} |\epsilon_{\alpha\sigma\sigma'}| \left(\langle n_{\mathbf{k}\sigma}^{a\dagger} \rangle - \langle n_{\mathbf{k}\sigma}^{b\dagger} \rangle + \langle n_{\mathbf{k}\sigma}^a \rangle - \langle n_{\mathbf{k}\sigma}^b \rangle \right). \quad (S6)$$

The numerical solution of the above equations give rise to the results shown in Fig. 2 of the main text.

MAGNETIC-FLUX INSERTION

To reduce finite-size effects, we follow ideas put forward in Ref. [50] and include in our simulations a single flux quantum traversing the lattice. In particular, the non-interacting part of the Hamiltonian reads:

$$H_0 = -t \sum_{\langle i,j \rangle} c_i^\dagger e^{\frac{2\pi i}{\Phi_0} \tau_z \int_i^{i+\delta} A(\mathbf{l}) \cdot d\mathbf{l}} c_j + \text{h.c.} \quad (S7)$$

Here, Φ_0 is the flux quantum, and $\mathbf{A}(\mathbf{l}) = -B(y, 0, 0)$ in the Landau gauge, with $B = \frac{\Phi_0}{|\mathbf{L}_1 \times \mathbf{L}_2|}$. That is, a single flux quantum traverses the lattice, lying in the x - y plane and being spanned by the vectors $\mathbf{L}_1 = L\mathbf{a}_1$ and $\mathbf{L}_2 = L\mathbf{a}_2$. Including τ_z preserves the time reversal symmetry, defined as $T^{-1} z c_{i\sigma\lambda}^\dagger T = \bar{z} i \tau_{\lambda\lambda'}^y c_{i\sigma\lambda'}^\dagger$, required to avoid the negative sign problem. Further details of the implementation of the flux can be found in Ref. [46].

By construction, the magnetic field vanishes in the thermodynamic limit. However the convergence of observables is greatly improved when including the flux. Here, we exemplify

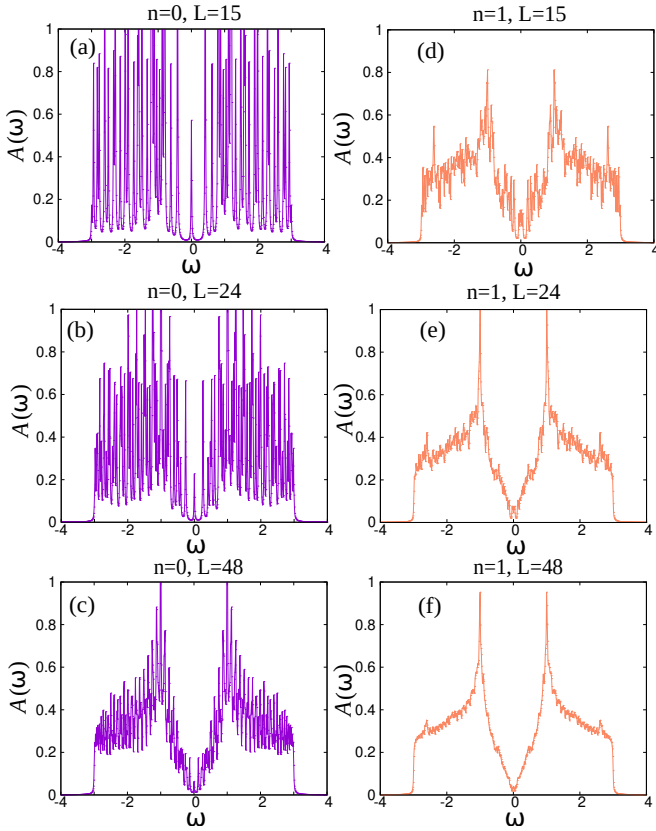


FIG. S1. Local density of states $N(\omega)$ of the tight-binding Hamiltonian H_0 (a)–(c) without magnetic flux insertion, $B = 0$, and (d)–(f) with magnetic flux insertion, $B = \frac{\Phi_0}{|L_1 \times L_2|}$, for different system sizes from $L = 15$ (top) to $L = 48$ (bottom). For the plot, we have used a broadening of $\delta = 0.01t$ and a discretization of the frequency range of $\Delta\omega = 0.01t$.

this by using the tight binding Hamiltonian H_0 on the honeycomb lattice. In Fig. S1, we present the finite-size fermion local density of states $N(\omega) = \frac{1}{\pi L^2} \sum_{\mathbf{k}} \text{Im Tr } G(\mathbf{k}, \omega)$. Panels (a)–(c) and (d)–(f) provide a comparison $N(\omega)$ without and with magnetic flux insertion, respectively. As apparent, the inclusion of the flux improves the quality of the density of states on finite-size lattices considerably.

This improvement, however, comes at a price, namely the breaking of translational symmetry along \mathbf{a}_1 and \mathbf{a}_2 . In fact, for our choice of the magnetic field, the magnetic unit cell corresponds to the full lattice. As a consequence, the momentum \mathbf{k} is no longer a good quantum number and the fermion Green’s function is not diagonal in this quantity. Nevertheless, we can still implement the Fourier transformation and define the fermion spectral function as $G(\mathbf{k}, \omega) = \frac{1}{L^2} \sum_{i,j} e^{-i\mathbf{k} \cdot (i-j)} G(i, j, \omega)$. In Panels (a)–(c) and (d)–(f) of Fig. S2, we plot the fermion spectral function $A(\mathbf{k}, \omega) = \frac{1}{\pi} \text{Im Tr } G(\mathbf{k}, \omega)$ without and with magnetic flux insertion, respectively. One observes that in the presence of the flux, $A(\mathbf{k}, \omega)$ is still dominated by the single-particle band observed in the absence of flux. However, novel features stemming from scattering between different momenta emerge

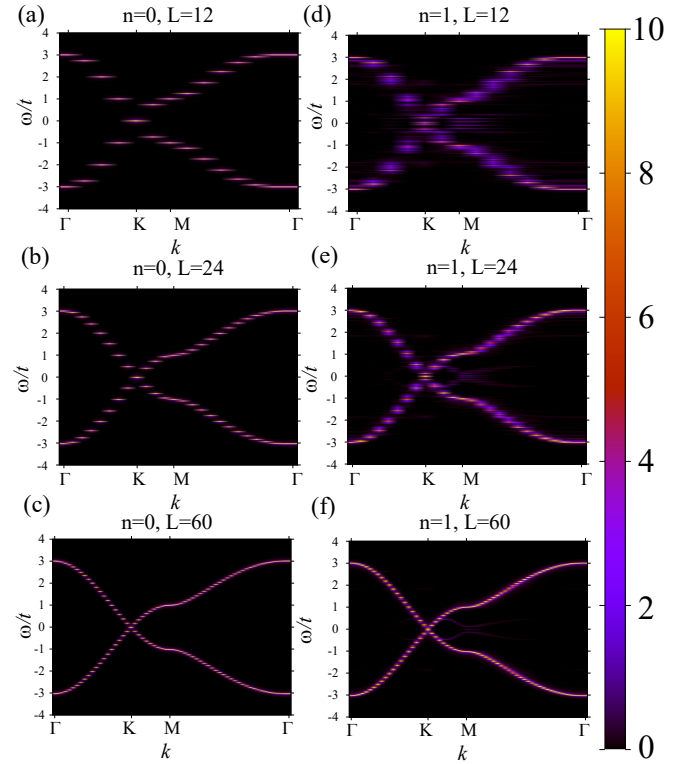


FIG. S2. Fermion spectral function $A(k, \omega)$ for tight-binding Hamiltonian H_0 (a)–(c) without magnetic flux insertion, $B = 0$, and (d)–(f) with magnetic flux insertion, $B = \frac{\Phi_0}{|L_1 \times L_2|}$, for different system sizes from $L = 12$ (top) to $L = 60$ (bottom).

at low energy and predominantly near the the high-symmetry point $M = (0, 2\pi/\sqrt{3})$. Clearly, as a function of system size, these features become weaker and ultimately disappear.

To show this explicitly, we study the quantity $N_p(\mathbf{k}) = \int_{\omega_1}^{\omega_2} A(\mathbf{k}, \omega) d\omega$, which integrates the spectral function at given momentum \mathbf{k} over a finite frequency range. We choose $\mathbf{k} = M$ and set $\omega_1 = -0.3$ and $\omega_2 = 0.3$, corresponding to a range of frequencies located well below the van Hove singularity at $\omega = \pm 1$. In Fig. S3, we show this quantity as a function of inverse system size $1/L$. As expected, we observe that this quantity vanishes in the thermodynamic limit.

GN-SO(3) TRANSITION: DATA-COLLAPSE ANALYSIS

Dimensionless RG-invariant quantities are the tool of choice to investigate critical phenomena. Here, we consider the quotient of correlation length ξ to the linear system size L . The correlation length can be extracted from the real-space two-point correlation function of the order-parameter field, $\tilde{S}(\mathbf{r})$, via

$$\xi^2 = \frac{1}{2d} \frac{\sum_{\mathbf{r}} |\mathbf{r}|^2 \tilde{S}(\mathbf{r})}{\sum_{\mathbf{r}} \tilde{S}(\mathbf{r})}, \quad (\text{S8})$$

where d corresponds to the spatial dimension.

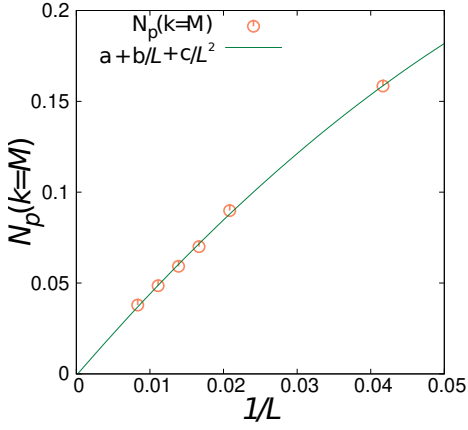


FIG. S3. Fermion spectral weight N_p at $\mathbf{k} = M$, integrated over finite frequency range $\omega \in [-0.3, 0.3]$, as function of $1/L$. The low-energy spectral weight is finite on finite-size lattices, but extrapolates to zero in the thermodynamic limit.

Following Ref. 30, we can use Eq. (S8), to define the correlation length as

$$\xi_{s,\kappa,\rho}^2(L) = \frac{\sum_{\substack{(-1+\kappa)L_1+1 \leq n_1 \leq \kappa L_1 \\ (-1+\rho)L_2+1 \leq n_2 \leq \rho L_2}} |n_1 \mathbf{a}_1 + n_2 \mathbf{a}_2|^2 S^{\text{SO}(3)}(n_1 \mathbf{a}_1 + n_2 \mathbf{a}_2)}{\sum_{\substack{0 \leq n_1 \leq L_1-1 \\ 0 \leq n_2 \leq L_2-1}} S^{\text{SO}(3)}(n_1 \mathbf{a}_1 + n_2 \mathbf{a}_2)} \quad (\text{S9})$$

on a finite-size system. In the above, \mathbf{a}_1 and \mathbf{a}_2 correspond to the lattice vectors of the honeycomb lattice. We consider lattices spanned by the vectors $L_1 \mathbf{a}_1$ and $L_2 \mathbf{a}_2$ with periodic boundary conditions. Since in our simulations $L \equiv L_1 = L_2$ is a multiple of 3 we can choose $\kappa = \rho = 1/3$. In the following discussion, we denote $R_\xi^{\text{SO}(3)}(L) = \xi_{s,\kappa=1/3,\rho=1/3}(L)/L$ as the RG-invariant quantity obtained in real space.

The correlation ratio [53] we discuss in the main text is equally an RG-invariant quantity and corresponds to an alternative estimate of ξ^2/L^2 . For instance, consider the Ornstein-Zernike form, $S^{\text{SO}(3)}(\mathbf{k}) \propto A/(\xi^{-2} + |\mathbf{k}|^2)$ where A is a constant. With this ansatz, the correlation ratio reads:

$$R_c^{\text{SO}(3)}(L) \equiv 1 - \frac{S^{\text{SO}(3)}(\mathbf{Q} + d\mathbf{k})}{S^{\text{SO}(3)}(\mathbf{Q})} = \frac{4\pi^2(\xi/L)^2}{1 + 4\pi^2(\xi/L)^2} = f(\xi/L) \quad (\text{S10})$$

The two RG-invariant quantities obey the following scaling form (for an explicit proof we refer the reader to Ref. [36]) close to the critical point

$$R_c^{\text{SO}(3)}(j, L) = g_1(L^z/\beta, (J - J_{c1}) L^{1/\nu}, L^{-\omega}) \approx f_0^R(jL^{1/\nu}) + L^{-\omega} f_1^R(jL^{1/\nu}) \quad (\text{S11})$$

$$R_\xi^{\text{SO}(3)}(j, L) = g_2(L^z/\beta, (J - J_{c1}) L^{1/\nu}, L^{-\omega}) \approx f_2^R(jL^{1/\nu}) + L^{-\omega} f_4^R(jL^{1/\nu}) \quad (\text{S12})$$

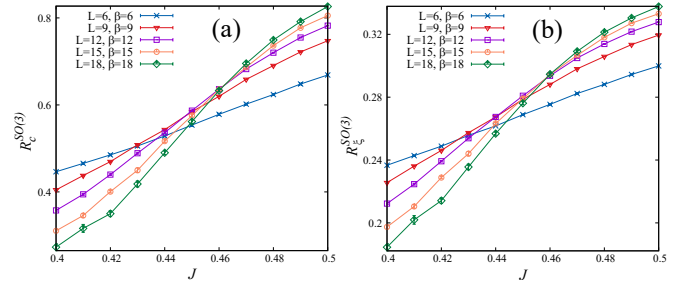


FIG. S4. RG-invariant quantities (a) $R_c^{\text{SO}(3)}$ and (b) $R_\xi^{\text{SO}(3)}$ as function of coupling constant J for different lattice sizes.

where $j = J - J_{c1}$ and g_1 and g_2 are scaling functions. Here, we assume that the dynamical exponent $z = 1$ and adopt a $\beta = L$ scaling. The term $L^{-\omega}$, $\omega > 0$, takes into account leading corrections to scaling that vanish as $L \rightarrow \infty$. For finite systems, corrections to scaling account for a drift in the crossing point of RG-invariant quantities as a function of system size. In Fig. S4, we show the RG-invariant quantities $R_c^{\text{SO}(3)}$ and $R_\xi^{\text{SO}(3)}$ for different lattice sizes L . Both curves show a common crossing point at $J \approx 0.46$ for system sizes $L \geq 12$. This observation suggests that corrections to scaling are weak in our FSS analysis and that we can neglect them in our analysis of the exponents. We perform a polynomial expansion of $f_0^R(jL^{1/\nu})$ and $f_2^R(jL^{1/\nu})$

$$R_c^{\text{SO}(3)}(j, L) = \sum_{n=0}^{n_{\max}} a_n j^n L^{n/\nu} \quad (\text{S13})$$

$$R_\xi^{\text{SO}(3)}(j, L) = \sum_{n=0}^{n_{\max}} b_n j^n L^{n/\nu} \quad (\text{S14})$$

and fit the data to these forms with $\{a_n\}$, $\{b_n\}$, critical exponent ν , and critical point J_c as fit parameters. Our results are summarized in Tables I and II. We adjust the expansion order n_{\max} as well as the minimum size L_{\min} to take into account systematic errors and corrections to scaling. We also present the χ^2/DOF value of the fit, where DOF refers to the number of degrees of freedom. In Table I, χ^2/DOF takes large values only for $L_{\min} = 6$ indicating the strong scaling correction for such small lattices. The best fit is obtained at $L_{\min} = 12$ and the results have a weak dependence on the expansion order for $n_{\max} \geq 3$. Our results based on the correlation ratio $R_c^{\text{SO}(3)}$ yield the estimates $J_{c1} = 0.461(1)$, $1/\nu = 0.906(35)$. In Table II, the numerical results based on the RG-invariant quantity $R_\xi^{\text{SO}(3)}$ are reported. The results at fixed $L_{\min} = 12$ are independent on the expansion order n_{\max} and we find consistent values, $J_{c1} = 0.458(1)$, $1/\nu = 0.937(21)$.

For the analysis of the bosonic, η_ϕ , and fermionic, η_ψ , anomalous dimensions, we numerically fit the FSS behavior of the SO(3) order parameter $m^2(j, L)$ and the quotient $Z(j, L)$. In the proximity of the critical point, these two quantities are

TABLE I. Results of fits of correlation ratio $R_c^{\text{SO}(3)}(L)$ close to J_{c1} . L_{\min} is the minimum lattice size taken into account in the fits. n_{\max} is the polynomial expansion order for the scaling function.

FSS analysis of $R_c^{\text{SO}(3)}(L)$ near J_{c1}				
L_{\min}	n_{\max}	J_{c1}	$1/\nu$	χ^2/DOF
6	2	0.444(3)	0.805(17)	47.121
	3	0.445(3)	0.867(16)	42.193
	4	0.445(3)	0.866(17)	42.165
	5	0.453(1)	0.883(17)	41.288
9	2	0.453(1)	0.827(18)	8.936
	3	0.454(1)	0.897(21)	7.366
	4	0.454(1)	0.893(21)	7.314
12	5	0.454(1)	0.894(21)	7.276
	2	0.461(1)	0.845(29)	1.835
	3	0.461(1)	0.906(35)	1.205
	4	0.461(1)	0.906(35)	1.127
	5	0.461(1)	0.901(37)	1.075

TABLE II. Results of fits of RG-invariant quantity $R_\xi^{\text{SO}(3)}(L)$ close to J_{c1} . L_{\min} is the minimum lattice size taken into account in the fits. n_{\max} is the polynomial expansion order for the scaling function.

FSS analysis of $R_\xi^{\text{SO}(3)}(L)$ near J_{c1}				
L_{\min}	n_{\max}	J_{c1}	$1/\nu$	χ^2/DOF
6	2	0.436(4)	0.894(9)	99.826
	3	0.435(4)	0.852(11)	98.463
	4	0.437(4)	0.918(12)	91.740
	5	0.437(4)	0.905(12)	91.486
9	2	0.449(2)	0.849(14)	11.432
	3	0.449(2)	0.850(13)	11.373
	4	0.449(2)	0.872(15)	10.662
12	5	0.449(2)	0.872(15)	10.629
	2	0.458(1)	0.937(21)	2.909
	3	0.457(1)	0.924(23)	2.762
	4	0.458(1)	0.935(26)	1.754
	5	0.458(1)	0.930(26)	1.684

expected to scale as:

$$\begin{aligned}
m^2(j, L) &= L^{2-d-z-\eta_\phi} g^m(L^z/\beta, (J - J_{c1}) L^{1/\nu}, L^{-\omega}) \\
&\approx L^{-1-\eta_\phi} (f^m(jL^{1/\nu}) + L^{-\omega} f_1^m(jL^{1/\nu})) \\
&= L^{-1-\eta_\phi} (\tilde{f}^m(R_{c/\xi}^{\text{SO}(3)}) + L^{-\omega} \tilde{f}_1^m(R_{c/\xi}^{\text{SO}(3)})) \quad (\text{S15})
\end{aligned}$$

$$\begin{aligned}
Z(j, L) &= L^{-\eta_\psi} g^z(L^z/\beta, (J - J_{c1}) L^{1/\nu}, L^{-\omega}) \\
&\approx L^{-\eta_\psi} (f^z(jL^{1/\nu}) + L^{-\omega} f^z(jL^{1/\nu})) \\
&= L^{-\eta_\psi} (\tilde{f}^z(R_{c/\xi}^{\text{SO}(3)}) + L^{-\omega} \tilde{f}^z(R_{c/\xi}^{\text{SO}(3)})). \quad (\text{S16})
\end{aligned}$$

In the last equalities of the above equations and in an attempt to minimize corrections to scaling, we have replaced $jL^{1/\nu}$ by $R_c^{\text{SO}(3)}$ or $R_\xi^{\text{SO}(3)}$. For $\beta = L$ scaling (appropriate for $z = 1$) and in the absence of corrections to scaling, the correlation ratios are functions of $jL^{1/\nu}$.

In Fig. S5, we show Lm^2 and Z as a function of $R_c^{\text{SO}(3)}$ and $R_\xi^{\text{SO}(3)}$. The decrease of Lm^2 and Z when increasing the system size L are a consequence of the anomalous dimensions η_ϕ and η_ψ in Eqs. (S15) and (S16). Omitting corrections to scaling and using a polynomial form for the scaling functions, we can determine the anomalous dimensions η_ϕ and η_ψ . Our results as function of L_{\min} and of the maximal expansion order n_{\max} are listed in Tables III and IV.

In Table III, we analyze the data as a function of $R_c^{\text{SO}(3)}$. The estimated value η_ϕ has small χ^2/DOF , which indicates a good agreement with the scaling form. The fit to the data in Table III yields a stable estimate of $\eta_\phi = 0.470(13)$ with respect to L_{\min} and to n_{\max} . The χ^2/DOF value of η_ψ in Table III shows a significant drop from $L_{\min} = 6$ to $L_{\min} = 9$, but is stable when varying $L_{\min} = 9$ to $L_{\min} = 12$. The dependence on the expansion power n_{\max} has virtually no effect on the estimated value of η_ψ . Table III shows that the fermion anomalous dimension is weakly dependent on L_{\min} and n_{\max} and takes the value $\eta_\psi = 0.292(10)$.

In Table IV, we analyze the data in terms of the RG invariant $R_\xi^{\text{SO}(3)}$. The scaling analysis of η_ϕ is less favorable than that of Table III. The χ^2/DOF values of η_ϕ in Table IV are larger when $n_{\max} < 4$. Although the estimated values vary as a function L_{\min} and n_{\max} , they are consistent with estimated values in Table III when taking into account the statistical uncertainty. The results of η_ψ have a stable small χ^2/DOF for $L_{\min} > 9$ and are not sensitive to the variation of n_{\max} . The estimated value of η_ψ in Table IV is consistent with the estimated value in Table III within statistical uncertainty.

GN-SO(3) TRANSITION: CROSSING-POINT ANALYSIS

In this section, we provide a consistency check of the above-estimated exponents using crossing points. The crossing-point analysis is a general and reliable way to extract the critical behavior [63]. The crossing point with size increment c is defined as the coupling $j_{c,R}(L)$ that satisfies $R_c^{\text{SO}(3)}(j_{c,R}(L), L) = R_c^{\text{SO}(3)}(j_{c,R}(L), L + c)$. As $L \rightarrow \infty$, the finite-size critical coupling $j_{c,R}(L)$ approaches the critical coupling J_c as

$$j_{c,R}(L) = J_c + AL^{-e} \quad (\text{S17})$$

where $e = 1/\nu + \omega$ and A is a nonuniversal constant [30]. Numerically, $j_{c,R}(L)$ can be estimated using a polynomial interpolation of the RG-invariant curves. Once we have estimated

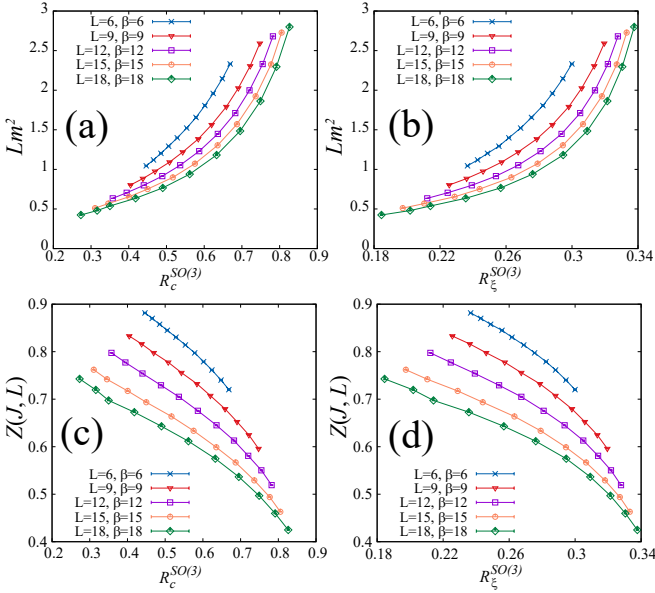


FIG. S5. FSS behavior of the SO(3) order parameter Lm^2 and quantity Z as a function of RG-invariant quantities $R_c^{\text{SO}(3)}$ and $R_\xi^{\text{SO}(3)}$ in the proximity of the metallic transition point J_{c1} .

TABLE III. Results of fits of the SO(3) order parameter $m^2(j, L)$ and $Z(j, L)$ as a function of the correlation ratio $R_c^{\text{SO}(3)}(L)$ close to J_{c1} . L_{\min} is the minimum lattice size taken into account in the fits. n_{\max} is the polynomial expansion order of the scaling function.

FSS analysis of $m^2(j, L)$ and $Z(j, L)$ via $R_c^{\text{SO}(3)}(L)$ near J_{c1}					
L_{\min}	n_{\max}	η_ϕ	χ^2/DOF	η_ψ	χ^2/DOF
6	2	0.464(11)	24.471	0.247(5)	119.198
	3	0.465(8)	11.419	0.248(6)	115.36
	4	0.467(7)	8.238	0.247(5)	109.831
	5	0.468(7)	7.931	0.248(6)	109.226
9	2	0.449(16)	25.179	0.284(4)	19.34
	3	0.456(8)	6.485	0.285(3)	16.659
	4	0.461(7)	4.644	0.285(4)	16.482
	5	0.461(7)	4.474	0.285(4)	16.169
12	2	0.457(35)	27.542	0.292(10)	21.329
	3	0.459(16)	5.33	0.292(9)	15.847
	4	0.470(13)	3.21	0.292(9)	15.614
	5	0.470(13)	3.039	0.292(10)	15.045

the finite-size critical coupling $j_{c,R}(L)$, it is straightforward

TABLE IV. Results of fits of SO(3) order parameter $m^2(j, L)$ and $Z(j, L)$ as a function of RG-invariant quantity $R_\xi^{\text{SO}(3)}(L)$ close to J_{c1} . L_{\min} is the minimum lattice size taken into account in the fits. n_{\max} is the polynomial expansion order of the scaling function.

FSS analysis of $m^2(j, L)$ and $Z(j, L)$ via $R_\xi^{\text{SO}(3)}(L)$ near J_{c1}					
L_{\min}	n_{\max}	η_ϕ	χ^2/DOF	η_ψ	χ^2/DOF
6	2	0.451(31)	374.096	0.233(5)	115.704
	3	0.482(15)	85.585	0.235(5)	102.444
	4	0.49(1)	36.467	0.234(5)	93.719
	5	0.500(8)	19.098	0.234(5)	93.321
9	2	0.435(49)	459.103	0.268(4)	27.286
	3	0.458(22)	88.106	0.269(3)	15.824
	4	0.486(12)	22.402	0.268(3)	15.443
	5	0.503(7)	8.291	0.268(3)	15.147
12	2	0.44(1)	478.842	0.278(12)	29.888
	3	0.433(44)	81.388	0.278(9)	14.69
	4	0.488(21)	16.614	0.277(9)	14.412
	5	0.506(13)	5.886	0.277(9)	15.045

to calculate the finite-size critical exponents using

$$\frac{1}{v(L, L+c)} = \frac{1}{\ln(r)} \ln \left\{ \frac{s(j_{c,R}(L), L+c)}{s(j_{c,R}(L), L)} \right\}, \quad (\text{S18})$$

$$\eta_\phi(L, L+c) = -\frac{1}{\ln(r)} \ln \left\{ \frac{m^2(j_{c,R}(L), L+c)}{m^2(j_{c,R}(L), L)} \right\} - 1, \quad (\text{S19})$$

$$\eta_\psi(L, L+c) = -\frac{1}{\ln(r)} \ln \left\{ \frac{Z(j_{c,R}(L), L+c)}{Z(j_{c,R}(L), L)} \right\}, \quad (\text{S20})$$

where $s(j, L) = \frac{dR_c^{\text{SO}(3)}(j, L)}{dJ}$ is the first-order derivative of the RG-invariant curve and $r = (L+c)/L$. The finite-size critical exponents discussed above scale to the correct exponent with a rate controlled by the leading-correction-to-scaling exponent ω ,

$$\frac{1}{v(L, L+c)} = \frac{1}{v} + dL^{-\omega}, \quad (\text{S21})$$

$$\eta_\phi(L, L+c) = \eta_\phi + gL^{-\omega}, \quad (\text{S22})$$

$$\eta_\psi(L, L+c) = \eta_\psi + kL^{-\omega}. \quad (\text{S23})$$

In Fig. S6, we summarize the crossing-point analysis of the critical coupling and the critical exponents, and compare with the result obtained from the data-collapse analysis. We consider two different size increments $c = 3$ and $c = 6$, with $r = (L+3)/L$ and $r = (L+6)/L$, respectively. Our data quality and size limitations hinder extrapolation to the thermodynamic limit. However, as shown in Fig. S6(a), the last two crossing points for $c = 3$ are very close to each other and to the estimate from the data-collapse analysis, suggesting weak corrections

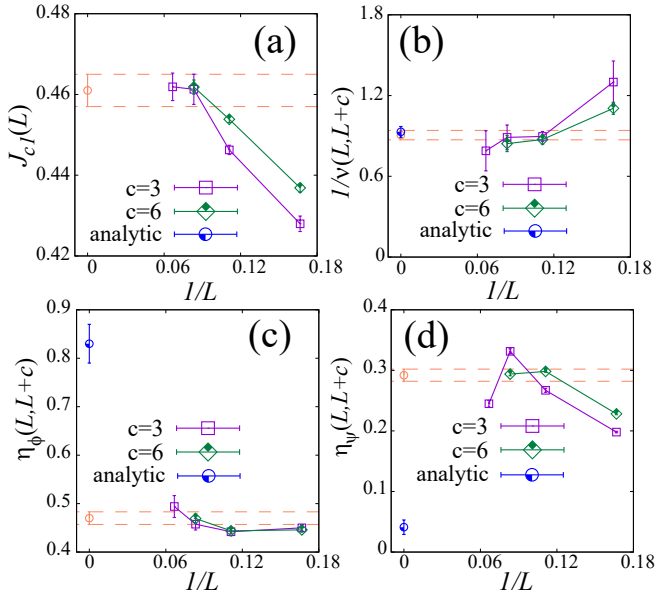


FIG. S6. System-size dependence of (a) critical coupling J_{c1} , (b) critical exponent $1/\nu$, (c) SO(3)-order-parameter anomalous dimension η_ϕ , and (d) fermion anomalous dimension η_ψ at the GN-SO(3) transition, as obtained from the crossing-point analysis. For comparison, the orange symbols and dotted lines in each panel indicate the estimates and statistical uncertainties, respectively, from the data-collapse analysis. The blue dots in (b-d) indicate the corresponding estimates from the analytical calculations of [39].

to scaling in the correlation ratio $R_c^{\text{SO}(3)}$ for $L \geq 12$. In Fig. S6(b), the finite size exponent $1/\nu(L, L+c)$ has large error bars that stem from the difficulty to compute the first-order derivative of the RG-invariant curve. As shown in Fig. S6(c), $\eta_\phi(L, L+c)$ shows weak increase as a function of system size. Within our estimated error bars, the largest size $\eta_\phi(L, L+c)$ is consistent with the value obtained from data collapse. In Fig. S6(d), $\eta_\psi(L, L+c)$ shows a smooth variation at $c = 6$ and the finite-size exponent again matches the estimate from the data-collapse analysis.

SO(3)-U(1) TRANSITION: DATA-COLLAPSE ANALYSIS

Our QMC data suggest the possibility of a second quantum critical point between the SO(3) semimetal and the U(1) insulator. If this is the case, it is worthwhile to estimate the critical exponents for this transition as well. In particular, the correlation-length exponent ν , as well as the critical coupling J_{c2} , are both expected to yield unique values when estimated from the two opposite sides of the transition, e.g., by using either the SO(3) or the U(1) order parameter. Following the same procedure as for the GN-SO(3) transition at J_{c1} , we extract the critical exponents and critical couplings from the two

different correlation ratios

$$R_c^{\text{SO}(3)}(j, L) = g_1(L^z/\beta, (J - J_{c2})L^{1/\nu}, L^{-\omega}) \approx f_0^R(jL^{1/\nu}) = \sum_{n=0}^{n_{\max}} a_n j^n L^{n/\nu} \quad (\text{S24})$$

and

$$R_c^{\text{U}(1)}(j, L) = g_1(L^z/\beta, (J - J_{c2})L^{1/\nu}, L^{-\omega}) \approx \tilde{f}_0^R(jL^{1/\nu}) + L^{-\omega} \tilde{f}_1^R(jL^{1/\nu}) = \sum_{n=0}^{n_{\max}} a_n j^n L^{n/\nu} + L^{-\omega} \sum_{m=0}^{m_{\max}} b_m j^m L^{m/\nu}. \quad (\text{S25})$$

The U(1) correlation curve shows a systematic drift of the crossing point that reflects the presence of a large leading-correction-to-scaling term $L^{-\omega} \tilde{f}_1^R$, see Fig. 5(b) of the main text. In our analysis we hence took this term into account. Our results are summarized in Tables V and VI. In Table V, the χ^2/DOF of the fit converge for $n_{\max} > 2$. The estimation of the critical point J_{c2} is stable and consistent with the crossing-point analysis. The estimated exponent $1/\nu$ is not sensitive to system size and we estimate $1/\nu = 1.673(58)$.

In Table VI, the error bars of the estimated exponent are larger due to the presence of the leading-correction-to-scaling term. Here we fix the expansion order $n_{\max} = 4$ and tune m_{\max} so as to improve the fitting quality. The quality of the fit is mildly improved with growing values of m_{\max} . Again, the estimated J_{c2} is stable and consistent with the crossing-point analysis. The estimated exponent $1/\nu$ converge to a stable value for $m_{\max} > 1$. In conclusion, the numerical fitting of $R_c^{\text{U}(1)}(j, L)$ yield an estimation $1/\nu = 1.458(642)$, that is consistent with the estimate obtained from $R_c^{\text{SO}(3)}(j, L)$, but with a larger error bar. Importantly, the two estimated values of J_{c2} match well.

SO(3)-U(1) TRANSITION: CORRELATION LENGTH

In Fig. S7, we present the real-space correlation length $\xi_{\text{SO}(3)/\text{U}(1)}$ near the SO(3)-U(1) transition at J_{c2} as obtained from the SO(3) and U(1) order parameters. We extract this quantity from the two-point correlation function following Eq. (S8). To be more precise, consider the U(1) correlation length in the SO(3)-ordered state corresponding to $J < J_{c2} = 1.007(17)$, Fig. S7(b). At a first-order transition, this quantity should saturate for increasing system size. At a continuous transition, it should be unbounded as J approaches the critical point from below, $J \nearrow J_{c2}$. For the accessible lattice sizes the data of Fig. S7(b) is consistent with the interpretation of a continuous transition.

Similarly, Fig. S7(a) shows the SO(3) correlation length as function of J . For a continuous transition, we expect this quantity to be unbounded in the U(1) ordered phase upon approaching the critical point from above, $J \searrow J_{c2}$. In this case, the data is harder to interpret, since the simulations on our largest lattice size, $L = 18$, could hint towards a saturation.

TABLE V. Results of fits of correlation ratio $R_c^{\text{SO}(3)}(L)$ close to J_{c2} . L_{\min} is the minimum lattice size taken into account in the fits. n_{\max} is the polynomial expansion order of the scaling function.

FSS analysis of $R_c^{\text{SO}(3)}(L)$ near J_{c2}				
L_{\min}	n_{\max}	J_{c2}	$1/\nu$	χ^2/DOF
6	2	1.001(2)	1.274(13)	62.649
	3	0.998(1)	1.732(18)	22.989
	4	0.997(1)	1.710(18)	19.812
9	2	1.007(1)	0.827(18)	66.139
	3	1.001(2)	1.706(29)	19.803
	4	1.000(2)	1.650(32)	16.797
12	2	1.011(15)	0.701(37)	74.78
	3	1.002(3)	1.692(60)	23.046
	4	1.001(3)	1.673(58)	20.249

TABLE VI. Results of fits of correlation ratio $R_c^{\text{U}(1)}(L)$ close to J_{c2} . L_{\min} is the minimum lattice size taken into account in the fits. m_{\max} is the polynomial expansion order of the leading correction scaling function. The main scaling function expansion order is fixed to $n = 4$.

FSS analysis of $R_c^{\text{U}(1)}(L)$ near J_{c2}					
L_{\min}	m_{\max}	J_{c2}	$1/\nu$	ω	χ^2/DOF
6	0	1.024(7)	0.786(120)	0.610(79)	26.311
	1	1.014(3)	1.241(32)	0.699(22)	19.219
	2	1.014(4)	1.502(321)	0.811(119)	16.88
9	0	1.022(6)	0.841(19)	0.525(55)	28.559
	1	1.014(3)	1.309(36)	0.582(60)	22.7
	2	1.011(5)	1.371(403)	0.824(135)	20.2
12	0	1.022(9)	0.800(26)	0.441(167)	27.162
	1	1.017(12)	1.096(202)	0.29(20)	25.88
	2	1.007(17)	1.458(642)	0.756(165)	15.662

TOPOLOGICAL DEFECTS OF SO(3) ORDER PARAMETER

In this section, we address the question if topological defects of the SO(3) order parameter, skyrmions, can localize electrons and thereby be important in understanding the criticality between the SO(3) semimetal and the U(1) insulator. In order to do so, we consider for an arbitrary static configuration of the SO(3) order parameter, $N_\alpha(\mathbf{r}_i)$, the mean-field Hamiltonian

$$H = -t \sum_{\langle ij \rangle \sigma} \left(c_{i\sigma}^\dagger c_{j\sigma} + \text{h.c.} \right) + \sum_{i\sigma} (-1)^{\tau_i} N_\alpha(\mathbf{r}_i) c_{i\sigma}^\dagger K_{\sigma\sigma'}^\alpha c_{i\sigma'} \quad (\text{S26})$$

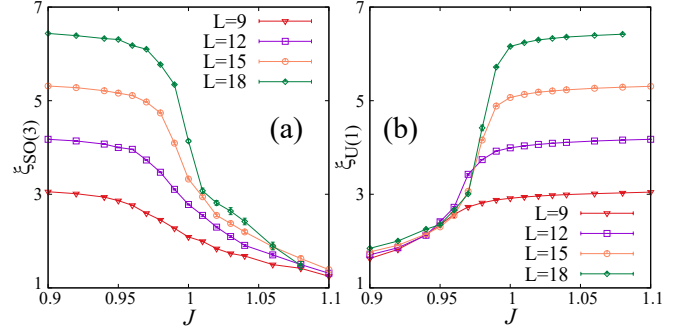


FIG. S7. Real-space correlation length ξ as function of J near the SO(3)-U(1) transition at $J_{c2} = 1.007(17)$, computed from Eq. (S8) using (a) the SO(3) and (b) the U(1) two-point correlators.

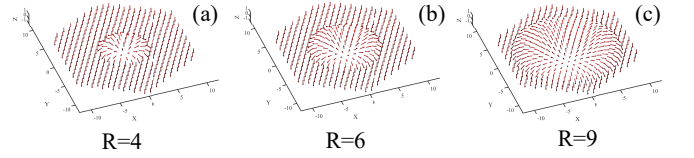


FIG. S8. Single-skyrmion configuration on $L = 21$ honeycomb lattice with skyrmion radius (a) $R = 4$, (b) $R = 6$, and (c) $R = 9$.

on the honeycomb lattice. Here, \mathbf{i} denotes a lattice site belonging to the unit-cell vector \mathbf{r}_i , which is taken to be the midpoint between the orbitals in the unit cell, $\tau_i = 1, 2$ correspond to the sublattice index, and $\sigma = 1, 2, 3$ corresponds to the SO(3)-spin-component index. To test our conjecture, we ignore the layer degree of freedom.

In the presence of periodic boundary conditions, we can consider the following skyrmion configuration

$$N(\mathbf{r}_i) = m_0 [\sin \theta(\mathbf{r}_i) \cos \phi(\mathbf{r}_i), \sin \theta(\mathbf{r}_i) \sin \phi(\mathbf{r}_i), \cos \theta(\mathbf{r}_i)] \quad (\text{S27})$$

with

$$\theta(\mathbf{r}_i) = \begin{cases} 2 \arcsin(r_i/R) & \text{for } r_i < R, \\ \pi & \text{for } r_i > R, \end{cases} \quad (\text{S28})$$

where $\phi(\mathbf{r}_i)$ is the azimuthal angle at position \mathbf{r}_i , and m_0 is the amplitude of the SO(3) order parameter. The radius of the skyrmion is determined by the parameter R . In Fig. S8, we present real-space skyrmion configurations for different values of R on an $L = 21$ lattice.

Our aim is to investigate the impact of the skyrmion on the local density of states (LDOS). In order to do so, we diagonalize the Hamiltonian of Eq. (S26) on the honeycomb lattice and choose $L = 90$ so as to reduce finite-size effects. We furthermore set $t = 1$ and $m_0 = 1$. In Fig. S9, we plot the LDOS, $N(\omega)$, at the center of the skyrmion. For small values of R , we observe distinct peaks in the LDOS. As R grows, they become less dominant and ultimately, the LDOS converges to that of the uniform field, Fig. S9(d). The data is hence consistent with the emergence of a discrete spectrum,

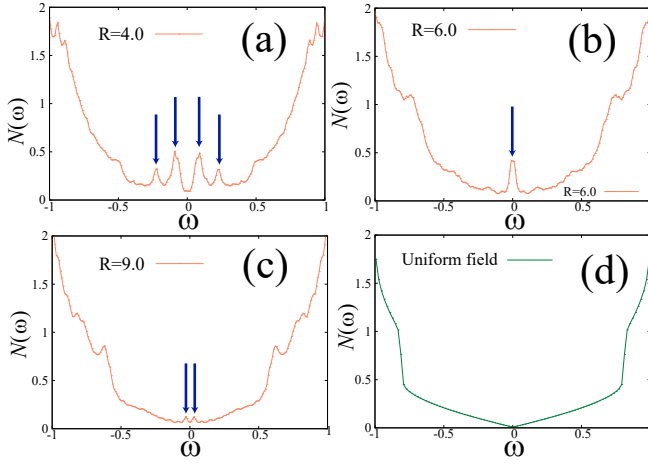


FIG. S9. Fermion local density of states at the center of the skyrmion with radius (a) $R = 4$, (b) $R = 6$, and (c) $R = 9$, using $L = 90$. The blue arrows point out the discrete-energy-level feature close to the Fermi energy. In (d), we plot the local density of states for a uniform field configuration $N(\mathbf{r}_i) = m_0(0, 0, 1)$ for comparison.

reminiscent of a particle in a box, generated by the skyrmion. The step from this *topological localization* to a theory of the phase transition necessarily involves the layer index. Here, we can conjecture that skyrmions on different layers bind, and that the localized states on the respective layers hybridize to form the U(1) order parameter.